High Speed Flow Through Silicon Nitride Nanopores as a Potential Dumb Hole

Sam Neale

Master of Science

McGill University, Montreal

A thesis submitted to McGill University in partial fulfillment of the degree of Master of Science

Contents

Abstract

Nanopores with diameters ranging from 30 nm to 50 *nm* were drilled in silicon nitride membranes using a transmission electron microscope (TEM) electron beam. High pressures of cold helium gas were applied to one side of the membranes to achieve flow through the nanopores. Mass flows for pressure gradients up to 1000 psi were measured with the goal of achieving transonic flow. Measured mass flows were compared to theoretical choked flow values and the flow speeds were deduced analytically. The ultimate goal of this work was to determine whether or not TEM drilled nanopores can act as de Laval nozzles and accelerate fluid to, or close to the speed of sound. While the silicon nitride nanopores do present some technical difficulties, we estimated that in our nanopores, Unruh temperatures on the order of 7×10^{-3} K were reached, leading to phonons being emitted at a rate in the range of 10^5 to 10^6 Hz.

Abrégé

Des nanopores de diamètres situés entre 30 et 50 nm ont été perçés dans des membranes de nitrure de silicium (amorphe) à l'aide d'un microscope électronique en transmission (MET). De hautes pressions de gaz d'hélium froid ont été appliquées d'un côté de la membrane permettant l'écoulement du fluide à travers le nanopore. Le débit de masse a été mesuré pour des differences de pressions allant jusqu'à 1000 psi, l'objectif étant d'atteindre un écoulement transonique. Les mesures ont été comparées à un modèle théorique et les vitesses d'écoulement ont été déduit analytiquement. Le but de ce projet est de déterminer si les nanopores perçés à l'aide du MET peuvent agir comme des tuyères de Laval et accélerer le fluide à des vitesses proches de celle du son. Bien que les nanopores utilisés présentent des difficultés techniques, il a été estimé qu'il permettraient d'observer une température de Unruh de l'ordre de 7×10^{-3} K, et les phonons seraient émis à une fréquence de l'ordre de 10^5 à 10^6 Hz.

Acknowledgements

I sincerely thank Professor Guillaume Gervais for bringing me to McGill and inspiring me with this project. His passion for science and research is something I will try to emulate in all of my future work.

I would like to thank Michel Savard and Guillaume Dauphinais for starting this project and providing me with much needed assistance throughout it. Thanks to Alex Maloney and Gil Holder for their insight into Hawking radiation and the Unruh effect. Thanks to Matei Petrescu and Pierre-Francois Duc for helping with calculations and simulations. I would also like to thank Richard Talbot for his help in designing various parts of the experimental setup, and Jean-Philippe Masse for his assistance with the TEM. Thanks to Ben Schmidt and to Bram Evert for their help with various software problems throughout this project.

Finally, thanks to all of my friends and familly for their support through everything. I would not have made it this far without them.

Dedication

This document is dedicated to all of the scientists and science teachers inspiring the next generation of researchers, and to all of those that inspired me.

List of Tables

List of Figures

Chapter 1

Introduction

1.1 Background of This Work

In 1976, William Unruh first proposed that accelerating bodies emit radiation [1]. Unruh's proposal followed up on the work done by Stephen Hawking on black hole evaporation [2]. Hawking discovered that black holes emit radiation when he applied quantum mechanics to the metric at the surface of a black hole. After applying a mathematical treatment similar to what was done by Hawking with black holes, but to accelerating bodies, Unruh found that accelerating bodies should emit radiation in the form of photons [3]. This radiation of photons from accelerating bodies is now called the *Unruh effect*. There also exists an analogue system where the Unruh effect radiates in phonons. While Hawking radiation has never been measured, the Unruh effect creates Hawking-like radiation that could be recreated in the laboratory.

While any accelerating body creates Unruh radiation, the corresponding Unruh temperatures are usually negligibly small. To provide a measurable Unruh effect, either the accelerations must be extremely large to create high Unruh temperatures, or the temperature of the fluid must be so low, as to allow low Unruh temperatures to be detected. There are several different approaches to detecting the Unruh effect. The most common approaches are creating sonic black holes in de Laval nozzles, in Bose-Einstein condensates, and using moving waves in water [4, 5, 6].

This work will specifically study sonic black holes in de Laval nozzles. A sonic black hole is a de Laval nozzle that accelerates a fluid to the speed of sound in the throat of the nozzle and to supersonic speeds beyond the throat. A sound wave emitted downstream from the throat cannot classically propagate back through the nozzle. Due to the Unruh effect, these sonic black holes, also known as dumb holes should still emit radiation. [3].

1.2 Goal of This Work

This work is the continuation of a project begun by Guillaume Dauphinais and Michel Savard [7, 8]. Dauphinais and Savard designed the experimental apparatus and used the same nanopore fabrication methods used here. This work will be intentionally brief on nanopore fabrication and stability as well as on the details of the experimental apparatus, as they were covered throroughly in Dauphinais, 2011 [7]. While these previous works focussed primarily on nanofluidics, this project will study high pressure flows and their relation to sonic black holes. The ultimate goal of this work is to determine whether transmission electron microscope (TEM) drilled nanopores can accelerate helium gas to the speed of sound and thus create, in principle, a sonic black hole.

Chapter 2 will cover the mathematical background of Hawking radiation and the Unruh effect, as well as some of the motivation behind this research. Chapter 3 will examine the physics of de Laval nozzles and choked flow, and explain the basic equations necessary for this research. Chapter 4 will provide a description of the experimental setup, the experimental procedure and the equipment used. Finally, Chapter 5 will summarize the mass flow data from the nanopores used, calculate the speeds reached and estimate the resulting Unruh temperatures and phonon emission rates.

Chapter 2

Black Holes and Sonic Black Holes

2.1 Black Holes

Black holes were first proposed by Karl Schwarzschild in 1916 as a solution to the field equations in Einstein's theory of General Relativity [9]. They were then interpreted as regions of space-time where gravity is so strong that nothing, not even light, could escape [10]. Based on early the understanding of black holes, four laws of mechanics were then derived to describe them. These four laws of black hole mechanics had a strong resemblance to the four laws of thermodynamics, but since black holes could not radiate and had no temperature, black hole mechanics could not be combined with thermodynamics into a complete theory. That changed in 1975 when Stephen Hawking formulated Hawking radiation, the thermal radiation of particles from the surface of a black hole [2, 11].

2.1.1 Hawking Radiation

Hawking radiation can be derived in many different ways. It was first derived by Stephen Hawking by applying quantum mechanics to the event horizon of a black hole [9]. A simple derivation of Hawking radiation starts with considering the Euclidean signature of a Schwarzschild black hole - that is, the transformation to imaginary time for a black hole with no angular momentum or charge. In natural units, where $c = G = 1$, the metric of a Schwarzschild black hole is given by

$$ds^2 = -\left(1 - R/r\right) dt^2 + \left(1 - R/r\right)^{-1} dr^2 + r^2 d\Omega^2 \tag{2.1}$$

where $R = 2M$ is the Schwarzschild radius of the black hole which depends on the mass M, r is the radial distance from the black hole and Ω is the solid angle.

It is clear that there is a singularity as one approaches the event horizon, *i.e.* when $r \to R$. This singularity, however, is only a coordinate singularity. This can be seen by making the following substitutions and studying some limits. First, taking the limit $r \to R + \varepsilon$, where ε is an infinitesimal distance, and then using a Taylor expansion to the first order, the metric simplifies to

$$ds^2 = -\frac{\varepsilon}{R} dt^2 + \frac{R}{\varepsilon} dr^2 + r^2 d\Omega^2. \tag{2.2}$$

Making a second substitution, $\eta = 2\sqrt{R\varepsilon}$, and using the Euclidean signature, $t = i\tau$, the metric becomes

$$ds^2 = \left(\frac{\eta^2}{4R^2}\right) d\tau^2 + d\eta^2 + r^2 d\Omega^2. \tag{2.3}$$

It is clear that under these substitutions, there is no longer a coordinate singularity. Now, defining $\phi = \tau/2R$, the metric further reduces to

$$ds^2 = \eta^2 d\phi^2 + d\eta^2 + r^2 d\Omega^2, \tag{2.4}$$

which is identical to the metric of flat space in polar coordinates if τ is cyclical, *i.e.* $\tau' \backsim \tau + 4\pi R$, or, $\tau' \sim \tau + \beta\hbar$. With this, one can define the time evolution as a Boltzmann factor with $\beta = 4\pi R/\hbar$. This Boltzmann factor can be interpreted as a probability density of a particle-antiparticle pair being created with one part inside the Schwarzschild radius and the other outside, free to escape. The Hawking Temperature is then given by

$$T = \frac{\hbar}{4\pi R k_B}. \tag{2.5}$$

In units where $c, G \neq 1$, the temperature is defined using the Schwarzschild radius expressed in terms of mass as

$$T = \frac{\hbar c^3}{8\pi G M k_B} = \frac{\hbar\kappa}{2\pi c k_B}, \tag{2.6}$$

where κ is the surface gravity of the black hole [12].

2.1.2 Difficulty of Observation

While Hawking radiation is generally accepted as a real, physical phenomenon, it has never been directly observed. The widespread acceptance is likely due to the fact that Hawking radiation can be derived in many different ways, using many different assumptions and all of these methods lead to the same result. Stephen Hawking initially derived Hawking Radiation by applying quantum mechanics to the event horizon of a black hole, but it has also been derived using Planck scale fluctuations, quantum field theories and various other methods [13]. While the theoretical foundation of Hawking radiation is strong, observation and experiment on this phenomenon are greatly lacking. Observation of Hawking radiation provides a unique difficulty due to the intrinsic elusiveness of black holes and due to low Hawking temperatures.

Many different black holes have been discovered, but all of them were observed indirectly. A common way to identify black holes is through the study of the objects orbiting them. If the period and radius of an orbiting object is measured, the mass of the central object can be calculated. The orbiting object also provides an upper bound on the radius of the massive object in the middle. Sufficiently massive, invisible objects can often be identified as black holes. Supermassive black holes that occur at the center of galaxies can be on the order of millions of solar masses and are easily identified if there is sufficient data on the stars surrounding them. Smaller black holes, however, are much more common, but can be difficult to distinguish from neutron stars if they have masses smaller than three solar masses. Black holes can also be identified in X-ray binary systems. These are systems where a black hole and another object are in close orbit with one another such that mass from the other object, often a star, can be transferred to the black hole. This accreted mass accelerates towards the black hole, emitting radiation, then disappears beyond the horizon. If the emitting region can be established as small and the mass of the accreting object can be found to be greater than three solar masses, then the object can be distinguished from a neutron star and identified as a black hole [14].

While all of these methods can identify an object as being a black hole, none of them identifies Hawking Radiation itself. One of the problems with observing Hawking radiation is that, as shown in Equation 2.6, the temperature is inversely proportional to the mass. While most astrophysical objects like stars or galaxies are more luminous when they are large, larger black holes emit less Hawking radiation than smaller black holes. Stefan-Boltmann's equation states that the power per unit area emitted by an object at a temperature T is given by

$$j = \sigma T^4, \tag{2.7}$$

while the surface area of a black hole increases as

$$A = \frac{4\pi (GM)^2}{c^4}. \tag{2.8}$$

Therefore, the power emitted is

$$P = jA \propto \left(\frac{1}{M}\right)^4 M^2. \tag{2.9}$$

This means that a black hole of ten solar masses emits 100 times less Hawking radiation than a black hole of one solar mass. Even a small black hole of one solar mass has a temperature of less than $10^{-7}K$, and creates too little radiation to be observed at astrophysical distances. Neglecting accretion, black holes have finite lifetimes, and it is in theory possible to observe the burst of radiation that would come from a black hole in its final moments, however, the lifetime of a black hole goes as

$$t \cong 10^{71} \left(\frac{M}{M_{sun}}\right)^3 s \tag{2.10}$$

and at the current age of the universe, this observation would require a black hole with a mass of 10^{12} kg ($5 \times 10^{-19} M_{sun}$) created shortly after the Big Bang [15]. The existence of such black holes is unknown, and the observation of these events are be unpredictable. With no current evidence for Hawking radiation coming from astrophysics, one must find other ways to simulate a black hole. One possible black hole analogue that could be created in the lab is in its acoustic analogue, the sonic black hole.

2.2 Acoustic Black Holes

Acoustic black holes, also known as dumb holes or sonic black holes, are analogues of astrophysical black holes in a very different physical system. While black holes are dense objects with gravitational fields that prevent light from escaping, acoustic black holes are fluid systems that achieve sonic flow speeds that prevent sound waves from escaping. Like black holes, dumb holes have a horizon. The sonic horizon is the point or cross section at which the fluid flow reaches the speed of sound. Sound waves created downstream from the sonic horizon cannot classically escape from a dumb hole, as they cannot achieve speeds greater than the flow speed as would be required to transmit the wave. Most importantly, dumb holes produce a sonic equivalent to Hawking radiation known as Unruh radiation [16]. Unruh radiation is the thermal emission of particles from an accelerating body.

2.2.1 Unruh Radiation

In the analogue system, Unruh temperatures can be derived in many different ways, similar to Hawking temperatures. A simple way to derive the Unruh effect is by considering a barotropic, irrotational fluid with zero viscosity, for simplicity. The continuity equation, *i.e.* the Euler equation and the barotripic equation of state, can the be written as

$$\frac{\partial \rho}{\partial t} + \overrightarrow{\nabla} \cdot (\rho \overrightarrow{v}) = 0, \tag{2.11}$$

$$\rho \left(\frac{\partial v}{\partial t} + \left(\overrightarrow{v} \cdot \overrightarrow{\nabla} \right) \overrightarrow{v} \right) = -\overrightarrow{\nabla} p, \tag{2.12}$$

and

$$p = p\,(\rho)\,, \tag{2.13}$$

respectively. One can then pick exact solutions, $p_o\,(t, x)$,$\rho_0\,(t, x)$, and $\psi_o\,(t, x)$, where $\overrightarrow{v} = \overrightarrow{\nabla} \psi$, with linear fluctuations p_1, ρ_1, ψ_1, etc. The equations of motion for these fluctuations can be combined to form the equation

$$\frac{\partial}{\partial t}\left(c_s^{-2}\rho_o\left(\frac{\partial\psi_1}{\partial t}+\overrightarrow{v_0}\cdot\overrightarrow{\nabla}\psi_1\right)\right)=\overrightarrow{\nabla}\cdot\left(\rho_0\overrightarrow{\nabla}\psi_1-c_s^{-2}\rho_0\overrightarrow{v_0}\left(\frac{\partial\psi_1}{\partial t}+\overrightarrow{v_0}\cdot\overrightarrow{\nabla}\psi_1\right)\right), \tag{2.14}$$

where c_s is the speed of sound. This equation is, in fact, identical to the equation

$$\frac{1}{\sqrt{-g}}\frac{\partial}{\partial x^\mu}\left(\sqrt{-g}\,g^{\mu\nu}\frac{\partial}{\partial x^\nu}\psi_1\right)=0, \tag{2.15}$$

where $g=\left[det\left(g^{\mu\nu}\right)\right]^{-1}$, for the metric

$$g^{\mu\nu}\left(t,\overrightarrow{x}\right)=\frac{1}{\rho_0\,c_s}\left[\begin{array}{ccc} -1 & \vdots & -v_0^j \\ \cdots & \ddots & \cdots \\ -v_0^i & \vdots & \left(c_s^2\delta_{ij}-v_0^iv_0^j\right) \end{array}\right]. \tag{2.16}$$

The inverse of this matrix is the so called acoustic metric,

$$g_{\mu\nu}^{acoustic}=\frac{\rho_0}{c_s}\left[\begin{array}{ccc} -\left(c_s^2-v_0^2\right) & \vdots & -\left[v_0\right]_j \\ \cdots & \ddots & \cdots \\ -\left[v_0\right]_i & \vdots & \delta_{ij} \end{array}\right] \tag{2.17}$$

[17].

This is the acoustic metric that was initially derived by Unruh. Following Unruh's procedure and using the change of time coordinates,

$$\tau=t+\int\frac{v_0^r\left(r\right)dr}{c_s^2-v_0^{r2}\left(r\right)}, \tag{2.18}$$

the metric can be written as

$$ds^2=\frac{\rho_0}{c_s}\left[\left(c_s^2-v_0^{r2}\right)d\tau^2-\frac{c_sdr^2}{c_s^2-v_0^{r2}}+r^2d\Omega^2\right]. \tag{2.19}$$

Figure 2.1: de Laval nozzle and acoustic black hole

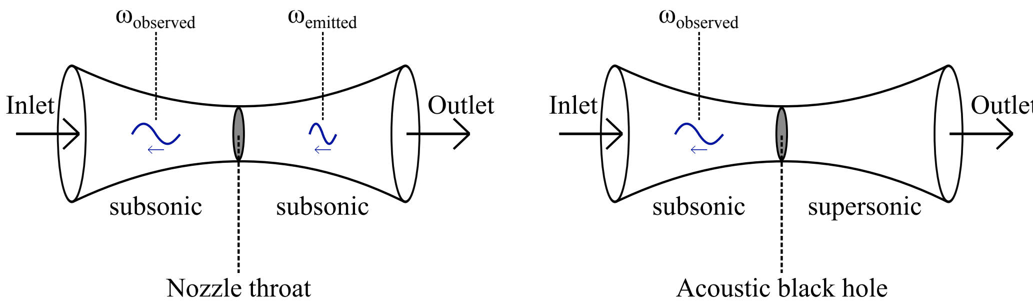

(a) Laval nozzle with subsonic flow. Phonons are redshifted and transmitted through the throat of the nozzle.

(b) Laval nozzle achieving sonic flow. Phonons are emitted from the throat of the nozzle.

Now, assuming that the velocity smoothly exceeds the speed of sound at $r = R$,

$$v_0^r = -c_s + \alpha\left(r - R\right) + \mathcal{O}\left(\left(r - R\right)^2\right), \tag{2.20}$$

the metric can be written as

$$ds^2 \approx \frac{\rho_0\left(R\right)}{c_s}\left[2c_s\alpha\left(r - R\right)d\tau^2 - \frac{dr^2}{2\alpha\left(r - R\right)}\right], \tag{2.21}$$

where the angular part was neglected. This conspicuously resembles the metric near the event horizon of a black hole, given by

$$d\hat{s}^2 = \frac{\left(\hat{r} - 2M\right)}{2M}d\hat{t}^2 - \frac{2M\,d\hat{r}^2}{\hat{r} - 2M} \tag{2.22}$$

[3].

Since a similar metric applies to both the case of an accelerating, irrotational fluid and to the region surrounding a black hole, similar physics will apply as well. This implies that, like a black hole, the accelerating fluid should also theoretically radiate. Making the appropriate substitutions in changing from a black hole in general relativity to an accelerating fluid, the Unruh temperature can be expressed as

$$T = \frac{\hbar g_H}{2\pi k_B c_s}, \tag{2.23}$$

where g_H here, is the sonic equivalent to the surface gravity given by

$$g_H = c_s \left(\frac{\partial v}{\partial x} \right) \Big|_{v=c_s} \tag{2.24}$$

[5]. In Equation 2.23, the speed of sound replaces the speed of light as the speed of the radiated waves and the fluid acceleration replaces the surface gravity of a black hole. It should be noted that the Unruh effect can be generalized to cases where no horizon is produced, and it is not necessary for a fluid to reach the speed of sound for Unruh Radiation to be created. Any accelerating fluid will radiate phonons, although most will radiate at such low temperatures, and thus be undetectable. The primary difference between sonic flows and mere high speed flows is the establishment of a trapped region and the creation of a sonic horizon in flows that become sonic [18].

2.2.2 Nanopores - Why Go Small

While there are many different approaches to creating sonic black holes, such as Bose-Einstein condensates or gravity waves in water, for example, this work will deal with creating a sonic black hole in a nanonozzle [16, 19]. De Laval nozzles are relatively simple tools used to create sonic and transonic flows, under the right conditions of pressure and shape. The reason for using small de Laval nozzles is to maximize the Unruh temperature. As is seen in Equations 2.23 and 2.24, the controlled variable in the Unruh temperature is the fluid acceleration. For a fluid moving through a Laval nozzle with a velocity which depends only on the z position in the direction of the flow, the

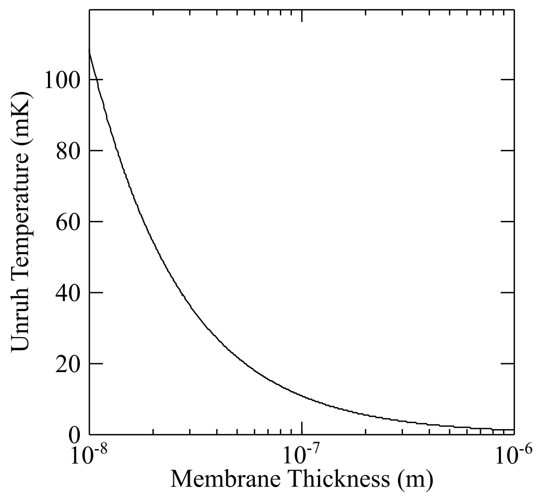

Figure 2.2: Theoretical Unruh temperature for sonic helium gas moving through a symmetrical de Laval nozzle with varying membrane thicknesses. The calculation assumes a constant fluid acceleration from a stationary fluid in the inlet to sonic flow in the throat.

velocity gradient must satisfy

$$\frac{c_s^2 - v^2}{v c_s^2}\left(\frac{dv}{dz}\right) = -\frac{1}{A}\frac{dA}{dz}, \tag{2.25}$$

using the Bernoulli equation and conservation of mass, where $A\,(z)$ is the the cross sectional areal of the nozzle. Assuming that the shape of the nozzle near the throat is approximately quadratic, *i.e.*

$$A(z) = A_0 + \beta z^2, \tag{2.26}$$

$$c_s^2 - v^2 = 2cz\frac{dv}{dz}, \tag{2.27}$$

and that the speed of sound is independent of pressure, which is reasonable if the pressure change is less than a factor of ten near the throat, the acceleration of the fluid must satisfy

$$\frac{dv}{dz} = c_s\sqrt{\frac{\beta}{A_0}} \tag{2.28}$$

[17, 20]. This indicates that for Laval nozzles of the same quadratic geometry

under the same conditions, the Unruh temperature of a nozzle with a diameter of 100 nm would be a factor 10^4 higher than that of a 1 mm nozzle. The power of phonons emitted also increases for smaller nozzles; the Stefan-Boltzmann law indicates that the power of phonons emitted is proportional to T^4 and A_o, so

$$Power = \sigma_{sound} T^4 A_0 \propto \frac{1}{r^2}. \tag{2.29}$$

The temperature decreases with increasing nozzle radius and length. The length controls the distance over which the fluid can accelerate and the radius must scale with the length in order for the de Laval nozzle to accelerate the fluid smoothly. Figure 2.2 shows how the Unruh temperature changes for a nanonozzle with varying membrane thicknesses, assuming that the fluid acceleration is constant and that the nozzle diameter scales with the membrane thickness. It is clear that in order to achieve higher Unruh temperatures, the scale of the de Laval nozzle must be small.

Chapter 3

Fluid Dynamics

The goal of this work is to examine an experimental setup and test its ability to achieve high accelerations in order to optimize Unruh temperatures, and its ability to produce sonic flows in order to create a sonic horizon. For sonic flows to be achieved, it will be shown that it is necessary to have a converging-diverging nozzle, otherwise known as a de Laval nozzle.

3.1 de Laval Nozzle

Fluid flow through a pipe can be described by the conservation of mass equation,

$$Q_m = \rho v A = constant, \tag{3.1}$$

where ρ is the density of the fluid, v is the velocity, and A is the cross sectional area of the pipe. This formula works for pipes even if the area is not constant, provided that the density and velocity are the average values at a given cross section and that there are no leaks or sources of additional fluid. Since this work will be dealing exclusively with the flow of cold helium gas, with a dynamic viscosity 1000 times lower than water, it is reasonable to use

Euler's equation for an inviscid fluid,

$$\left(\vec{v} \cdot \vec{\nabla}\right) \vec{v} = -\frac{1}{\rho}\vec{\nabla} P. \tag{3.2}$$

For flow along a streamline,

$$v \, dv = -\frac{dP}{\rho}, \tag{3.3}$$

and using the definition of the speed of sound,

$$\frac{dp}{d\rho} = c_s^2, \tag{3.4}$$

it is possible to describe the mass flux, $j = \rho v$, by

$$\frac{dj}{dv} = \rho \left(1 - \frac{v^2}{c_s^2}\right). \tag{3.5}$$

Differentiating the conservation of mass equation yields

$$\frac{1}{v}\frac{dv}{dz} + \frac{1}{A}\frac{dA}{dz} + \frac{1}{\rho}\frac{d\rho}{dz} = 0, \tag{3.6}$$

where the flow here is chosen to be moving in the z direction. Combining Equations 3.3, 3.4, and 3.6, it is possible to write

$$\frac{1}{v}\left(1 - \frac{v^2}{c_s^2}\right)\frac{dv}{dz} = -\frac{1}{A}\frac{dA}{dz} \tag{3.7}$$

[21]. This equation shows why it is necessary to use a converging-diverging nozzle to achieve supersonic speeds. For $v < c_s$, the two sides of Equation 3.7 have opposite signs, indicating that as the area decreases, the velocity increases. The sign of the left hand side changes once $v > c_s$. This implies

that if the speed of sound is achieved in the throat of the nozzle, then the flow accelerates to supersonic speeds beyond the throat of the nozzle if the nozzle widens. It is also worth noting that a nozzle can only achieve $v = c_s$ in the throat where $dA/dz = 0$. A simple converging nozzle cannot achieve supersonic speeds.

If no shockwave occurs in the flow, then helium gas can be treated as an ideal gas. Using the ideal gas law along with the Bernoulli equation, the basic flow properties can be solved for exactly for the inlet pressure, density and temperature, P_0, ρ_0, and T_0, respectively. The inlet values, where $v = 0$, can be found to be

$$P = P_0 \left[1 - \frac{1}{2}(\gamma - 1)\frac{v^2}{c_s^2}\right]^{\frac{\gamma}{\gamma-1}}, \tag{3.8}$$

$$\rho = \rho_0 \left[1 - \frac{1}{2}(\gamma - 1)\frac{v^2}{c_s^2}\right]^{\frac{1}{\gamma-1}}, \tag{3.9}$$

and

$$T = T_0 \left[1 - \frac{1}{2}(\gamma - 1)\frac{v^2}{c_s^2}\right], \tag{3.10}$$

where $\gamma = c_P/c_V$ is the specific heat ratio, which is $5/3$ for helium. This model assumes that helium can be treated as a perfect gas, that the flow is isentropic and that there is steady flow. The velocity of the flow can then be computed to be

$$v(z) = \sqrt{\frac{2\gamma}{\gamma - 1}\frac{P_0}{\rho_0}\left[1 - \left(\frac{P(z)}{P_0}\right)^{\frac{\gamma-1}{\gamma}}\right]} \tag{3.11}$$

if the downstream pressure $P(z)$ is known [23].

If the downstream pressure is not known, another approach can be used to calculate the velocity of the flow. Given the equation of conservation of mass, Equation 3.1 and the formula for the speed of sound,

$$c_s = \sqrt{\gamma R_s T} \tag{3.12}$$

where R_s is the specific gas constant, the mass flow can be found using

$$Q_m = \rho AM\sqrt{\gamma R_s T} \tag{3.13}$$

where $M = v/c_s$, is the Mach number. Furthermore, using the perfect gas law,

$$\rho = \frac{P}{R_s T} \tag{3.14}$$

and the isentropic relation,

$$P = P_0 \left(\frac{T}{T_0}\right)^{\frac{\gamma}{(\gamma-1)}}, \tag{3.15}$$

both of which are reasonable assumptions for cold helium gas, the mass flow can be calculated using

$$Q_m = \frac{AP_0}{\sqrt{T_0}}\sqrt{\frac{\gamma}{R_s}}M\left(1+\frac{\gamma-1}{2}M^2\right)^{\frac{-(\gamma+1)}{2(\gamma-1)}}. \tag{3.16}$$

Using the isentropic relation for temperature,

$$\frac{T}{T_0} = \left(1+\frac{\gamma-1}{2}M^2\right)^{-1}, \tag{3.17}$$

the mass flow can be defined entirely in terms of the Mach number and the initial conditions of the inlet of the nozzle,

$$Q_m = \frac{AP_0}{\sqrt{T_0}}\sqrt{\frac{\gamma}{R_s}}M\left(1+\frac{\gamma-1}{2}M^2\right)^{\frac{-(\gamma+1)}{2(\gamma-1)}}. \tag{3.18}$$

This equation can be used to calculate the Mach number of the flow in the throat when the mass flow, initial pressure and initial temperature are known. Once the Mach number is known, Equation 3.17 can be used to find the temperature, Equation 3.12 can be used to find the speed of sound, and the combination of the speed of sound with the Mach number allows calculation of the speed through the throat of the nozzle [22].

3.2 Choked Flow

As can be seen from Equation 3.5, the mass flow maximizes when $v = c_s$. This means that there is a maximum flow that can be achieved by a nozzle with a specific configuration. These flows are refered to as *choked flows*. Increasing the upstream pressure of a choked flow will not increase the flow speed in the throat of the nozzle. The properties of these choked flows can easily be computed and thus provide a check if sonic flow has been achieved. Given the equations in Section 3.1, the following properties can be derived for the throat of a choked flow:

$$T_* = T_0 \left(\frac{2}{\gamma + 1} \right), \tag{3.19}$$

$$P_* = P_0 \left(\frac{2}{\gamma + 1} \right)^{\frac{\gamma}{\gamma - 1}}, \tag{3.20}$$

$$\rho_* = \rho_0 \left(\frac{2}{\gamma + 1} \right)^{\frac{1}{\gamma - 1}}, \tag{3.21}$$

$$c_* = c_0 \sqrt{\frac{2}{\gamma + 1}}. \tag{3.22}$$

These quantities refer to the temperature, pressure, density and speed of sound as measured in the throat of a nozzle which reaches sonic flow. The mass flow is then

$$Q_* = \rho_* c_* A_* = \sqrt{\frac{\gamma m}{k T_o}} \left(\frac{2}{\gamma + 1} \right)^{\frac{1+\gamma}{2(\gamma - 1)}} A_* P_0 \tag{3.23}$$

[23]. This is the best expermental test to determine whether the speed of sound has been achieved in a nozzle as it requires the fewest assumptions and allows a direct comparison of mass flows [23]. If the flow is below the speed of

sound, then Equation 3.18 should be used to calculate the flow speed.

Unfortunately, neither of these methods provide information on the fluid acceleration. This work will then assume constant acceleration from the entrance to the nozzle to the throat of the nozzle. While the inlet velocity can reasonably be treated as being zero, assuming a constant acceleration will underestimate the maximum achieved Unruh temperatures. A more accurate approach would be to numerically calculate the acceleration of the fluid using computational fluid dynamics, *i.e.* solving numerically for the Navier-Stokes equation for a given throat geometry. This work is currently on-going.

Chapter 4

Experiment

4.1 Samples

The samples used in this experiment were transmission electron microscope (TEM) wafers purchased from Silson Ltd. These samples consist of a small silicon nitride window on a Si[100] wafer. The wafers are 200 μm thick while the silicon nitride membranes used were 30, 50, 75, and 100 nm thick. Small windows were used to ensure that the total force on the membranes was small even at high pressures, allowing pressures of 900 to 1100 psi[1] to be applied before the membranes risked being damaged.

4.2 Nanopore Fabrication

All nanopores in this experiment were drilled using a transmission electron microscope. Using a TEM, nanopores can be drilled by focussing the electron beam on a silicon nitride membrane [24]. This technique allows real time visualization of the nanopore as well as subnanometer image resolution. TEM drilling also allows precise size control of the nanopore as a hole can be shrunk or enlarged once drilled [25, 26]. By lowering the beam intensity, the silicon

[1]In this work, the non-SI unit of pressure "psi" will be used for historical reasons

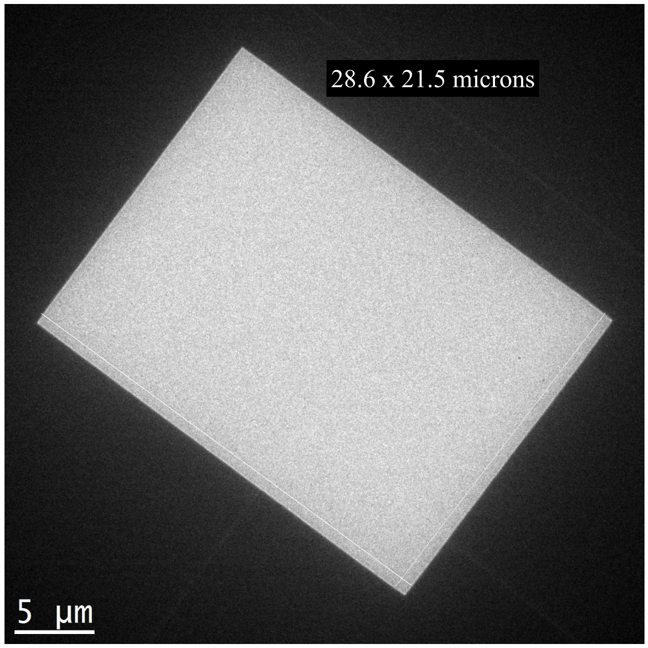

Figure 4.1: Silicon nitride membrane prior to drilling. Image taken with a JEM-2100F transmission electron microscope.

nitride on the surface can be fluidized, allowing matter to flow towards the open pore in a free energy minimization process, provided that the diameter of the pore is less than half the thickness of the membrane. Studies have been done to determine the three dimensional structure of pores drilled using a transmission electron microscope and found that matter is removed on both sides of the membrane, thus creating an hourglass shape [26]. Longer exposures, however, create a more cylindrical nanopore. This hourglass shape is a good starting point for a nano-scale de Laval nozzle. Figure 4.2b shows the shape of the nanopore extracted from the TEM picture shown in Figure 4.2a.

The profile is inferred using the brightness of different points of the image and averaging all points with the same radial distance from the center of the nanopore. The pointed shape at the narrowest part of the nanopore is therefore likely an artifact caused by the averaging of different points and the asymmetry of the pore. This method of finding the profile is not sufficient if the precise shape of the nanopore is to be used in calculations, but it is

Figure 4.2: 40 nm nanopore

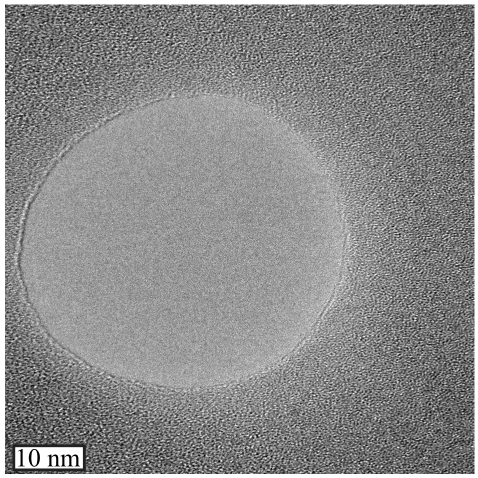

(a) TEM image of a nanopore with dimensions 43.7×39.4 nm

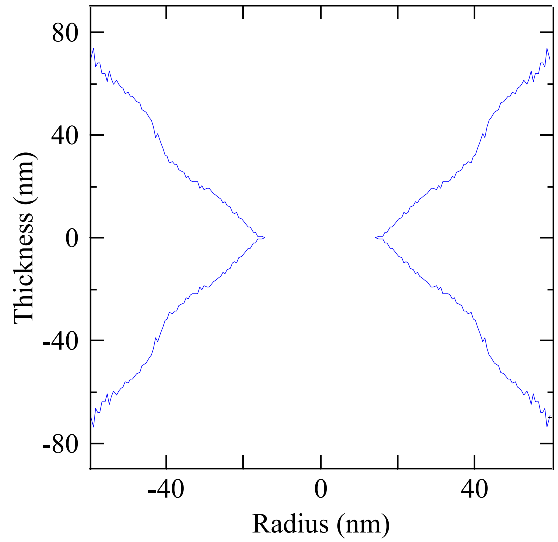

(b) Cross section of the nanopore shown in (a) constructed using relative electron intensity

nevertheless sufficient to establish the hourglass shape of the nanopore and provide the diameter of the nanopore opening.

4.3 Gas Handling System

In our flow experiment, pressure is applied to the nanopores using a gas handling system that contains helium gas. The gas handling system consists of a helium reservoir, stainless steel capillaries, two dipsticks submerged in liquid nitrogen, pressure gauges, valves, several cold traps, a vacuum pump or mass spectrometer and a cell to contain the nanopores.

4.3.1 Gas Flow

Capillaries connect each part of the gas handling system in order to transport helium from one part of the gas handling system to another. When experiments are not being done, the gas handling system is connected to a turbo vacuum pump in order to clear the capillaries of helium, which could be detected during experiment. Between the vacuum pump and the rest of the gas handling system is a cold trap, which consists of charcoal submerged in liquid nitrogen. The cold traps freeze any contaminants that might enter the gas handling system and prevent them from clogging the capillaries.

To perform experiments, the turbo vacuum pump is replaced by a mass spectrometer. The mass spectrometer has a vacuum pump of its own in order to maintain pressure gradients. Gas is allowed into the capillaries from the helium reservoir, directed by the valves, through a cold trap, through the cell which contains a nanopore and out to the mass spectrometer which then reads the volume flow.

4.3.2 Vacuum Pumps

This experiment used a two stage vacuum pump system. The primary pump was a Varian TV 700 turbo-molecular pump which was then backed by an Edwards 5 two stage rough pump. The turbo-molecular pump is not intended for use at atmospheric pressures, thus necessitating the rough pump in order to reduce the initial pressure. This pump system is used between every experimental test in order to remove as much helium from the gas handling system as possible, allowing experiments to being at low pressures.

4.3.3 Experimental Cell

The experimental cell is used to connect the silicon nitride membranes containing nanopores to the gas handling system. It is composed of stainless steel and is designed to function and be leak free at room temperature and while submerged in liquid nitrogen at 77 K. The main components of the cell are two stainless steel cylinders with brass adapters that connect to the capillaries of the gas handling system. There are then holes through the center of the cylinders to connect the capillaries to a small space in the middle where the sample will be placed. O-rings are placed at each connection to ensure

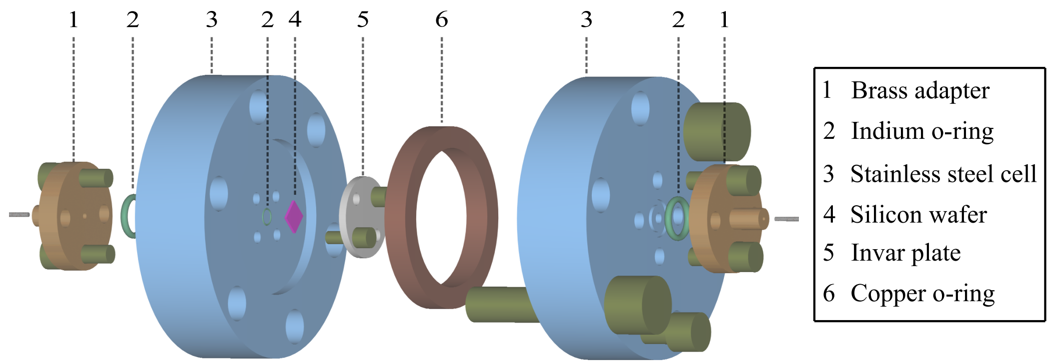

Figure 4.3: Experimental cell with all parts labelled.

that there are no leaks.

To assemble the experimental cell with a membrane, a small indium o-ring is placed in a slight groove around the hole on the bottom cylinder. The silicon wafer is then placed on top of the indium and a small invar plate can be screwed in carefully to hold the membrane in place and compress the indium, thus creating a seal to ensure that any helium entering the cell can only pass though the nanopore. The plate also contains a small hole through the middle, allowing helium to flow towards the membrane. Around the plate is another small groove in which a copper o-ring is placed. The top cylinder can then be placed on top of the bottom half and screwed in, compressing the copper ring and again creating a seal to keep air from entering the cell and to keep helium from escaping. Once the cell is assembled, leak checks are performed at both room temperature and at $77K$.

4.4 Experimental Procedure

In this work, experiments were run with the experimental cell at room temperature and 77 K, but all high pressure tests were done at 77 K. All experiments began at low pressure, with the turbo vacuum pump attached. This ensured that, as much as possible, all helium detected is coming through the nanopore rather than being residual helium in the capillaries between the nanopore and the mass spectrometer. The turbo vacuum pump is usually left on overnight for best results.

Once the mass spectrometer is attached, all valves are opened between the nanopore and the mass spectrometer so that a background reading can be obtained. It usuallly takes 1.5 to 2 hours to obtain a stable background reading. At this point, the mass spectrometer is zeroed so that the reading shown is due to flow through the nanopore alone.

To begin measurements, the valves are controlled to allow a small amount of helium into the capillaries above the nanopore. It takes approximately 7 minutes for the gas to move through the nanopore and obtain a stable pressure and flow. Once stable flow is achieved, the pressure is read using the pressure gauge above the cell and the flow is read from the mass spectrometer. These values are written in a lab book, along with the room temperature, while the data from the mass spectrometer is continuously displayed on a computer to best determine when stable flow is achieved.

After the first measurement is taken, the valves are once again controlled to allow the pressure to increase above the nanopore. This process continues, generally by increasing the pressure by factors between 1.2 and 1.5 as to provide even point spacing on logarithmic plots, until the pressure above the nanopore reaches that of the helium reservoir (78 psi). Once this pressure is achieved, the dipsticks need to be used to increase the pressure further. One of the dipsticks is moved from the liquid nitrogen dewar to a liquid helium dewar. Gas from the capillaries and the helium reservoir is then allowed to flow into the dipstick. The low temperature of the helium reduces the pressure in the dipstick, allowing more helium mass to enter the same volume. The valves around the dipstick are then closed to prevent helium flow and the dipstick is moved back into liquid nitrogen, thus increasing the temperature of the gas as well as the pressure. This high pressure helium is then allowed to flow through the nanopore. This process is repeated until no more helium can be extracted from the helium reservoir, often around 1100 psi.

After a complete set of data has been taken, the experiment is done in reverse. This allows additional data to confirm the validity of the first experiment, allows the helium to move back into the reservoir for later experiments and also allows more precise control of helium pressures than the initial experiment. Helium pressures are reduced by once again moving the dipstick from the liquid nitrogen dewar to the liquid helium dewar. The valves are opened slightly to allow helium to flow slowly from above the nanopore into the dipstick. Like in the first experiment, 7 minutes are allowed to pass with the valves above the nanopore closed to allow the pressure and flow to stabilize before data points are taken. Data points are once again taken at set intervals until no more pressure can be extracted from above the nanopore. Once the experiment is complete, the dipstick is moved back to liquid nitrogen to allow the helium to move back into the helium reservoir.

This experiment takes time and complete data sets often take more than one day. This causes a few problems. For one, other experiments take place in the lab which often release helium is into the air, although never while data is being taken. Because of this, the helium levels in the room change from day to day and this cannot be accounted for after taking the initial background reading. The other problem is that, while the room temperature is taken throughout the experiment to convert volume flows as read from the mass spectrometer into mass flows, the mass spectrometer itself creates its own heat. When data is taken at the start of the day, the mass spectrometer is cool and thus it is reasonable to assume that the helium measured in the mass spectrometer is at room temperature, but as the experiment progresses, the mass spectrometer can heat the helium beyond room temperature. While this does not cause large errors in the calculations made based on the measured volume flows, it can create slight offsets that are visible in plots of the data.

Chapter 5

Results

5.1 Low Pressure Tests

Low pressure tests were done on all samples used, either separately or as part of high pressure tests. At low pressures, it is simple to determine the radius of the nanopore used directly from the measured volume flow. This allows confirmation that the observed flow is indeed through the nanopore alone and that there are no external leaks.

The conductance is defined by

$$G = \frac{Q_m}{\Delta P} \simeq \frac{Q_m}{P}, \tag{5.1}$$

where Q_m is the mass flow, since one side is kept under vacuum [27]. The conductance is constant if the Knudsen number,

$$K_n = \frac{\lambda}{D}, \tag{5.2}$$

is greater than $\sim$10. In equation 5.2, D is the diameter of the nanopore, and

λ is the mean free path, defined by

$$\lambda = \frac{k_B T}{\sqrt{2}\pi d^2 P}. \tag{5.3}$$

Here, T is the temperature in the experimental cell and d is the diameter of a helium atom. The mass flow can be calculated from the volume flow measured in the mass spectrometer using the equation

$$Q_V = \frac{k_B T_{local}}{m} Q_m. \tag{5.4}$$

In this case, T_{local} is the temperature where the volume flow is being measured. For this experiment T_{local} is the temperature inside the mass spectrometer.

In the Knudsen regime, *i.e.*, for $K_n \gtrsim 10$, the conductance of a cylindrical pore is known to be

$$G = K\sqrt{\frac{\pi m}{2k_B T}} R^2, \tag{5.5}$$

for $K_n > 10$, where r is the radius of the nanopore and K is the Clausing factor [28]. The Clausing factor is a constant determined by the length to radius ratio of a cylindrical hole. It corrects the conductance for holes which can not be considered either pin holes ($L/R \to 0$) or infinitely long pipes ($L/R \to \infty$) [29].

L/R	K
0.1	0.952
0.2	0.909
0.5	0.801
1	0.672
2	0.514
5	0.311
10	0.191

Table 5.1: Clausing factors for varying length to radius ratios.

In the case of nanopores drilled with a TEM, the values in Table 5.1 can

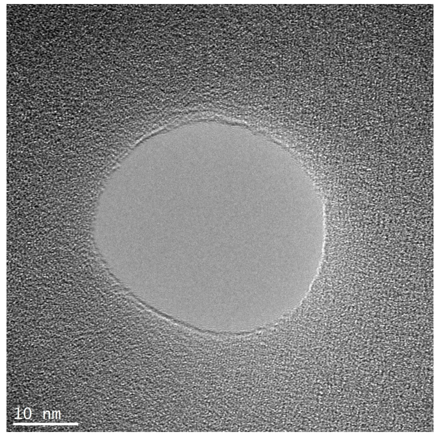

Figure 5.1: Image of a 32.4×35.2 nm nanopore in a 100 nm thick membrane taken with a TEM.

α	L/R						
deg.	0.1	0.2	0.5	1.0	2.0	5.0	10.0
0	0.952399	0.909215	0.801271	0.671984	0.514231	0.310525	0.190940
1	0.954079	0.912490	0.808852	0.685401	0.536021	0.345995	0.236829
5	0.960373	0.924763	0.837261	0.735659	0.617560	0.478646	0.408600
10	0.967347	0.938350	0.868615	0.790779	0.705799	0.617242	0.580298
20	0.97865	0.96027	0.91851	0.87642	0.83704	0.80558	0.79641
30	0.98691	0.97614	0.95344	0.93338	0.91771	0.90814	0.90611
40	0.99268	0.98701	0.97619	0.96806	0.96288	0.96046	0.96008
50	0.9964	0.9939	0.9896	0.9870	0.9857	0.9852	0.9851
60	0.9986	0.9977	0.9965	0.9959	0.9957	0.9956	0.9955
70	0.9996	0.9994	0.9993	0.9992	0.9992	0.9992	0.9991
80	1.0000	1.0000	1.0000	1.0000	1.0000	1.0000	1.0000
89	1.0000	1.0000	1.0000	1.0000	1.0000	1.0000	1.0000

Table 5.2: Clausing Factors For Conical Orifices [29]

only be used as a guide. This is because the hourglass shape of the nanopores changes the effective length to radius ratio [30]. The shape can be taken into account using the angle of the opening, α.

Calculating the expected conductance for a nanopore of given dimensions ensures that all measured flow is coming through the nanopore rather than through leaks in the indium seal. Any such leaks would be on the order of microns and easily distinguishable from flow through nanopores. Measurements of the conductance can also indicate whether the nanopore has grown

Figure 5.2: Measured flow through the nanopore displayed in Figure 5.1

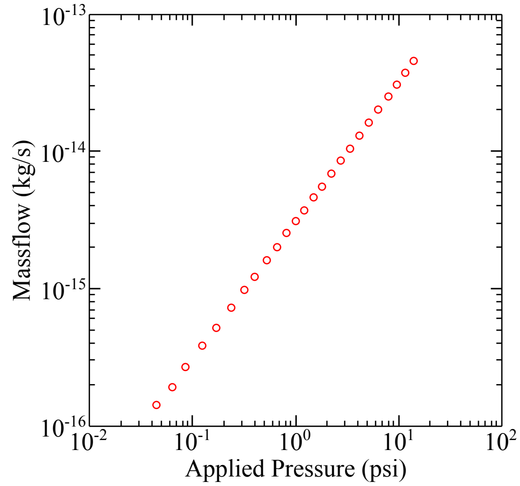

(a) Mass flow.

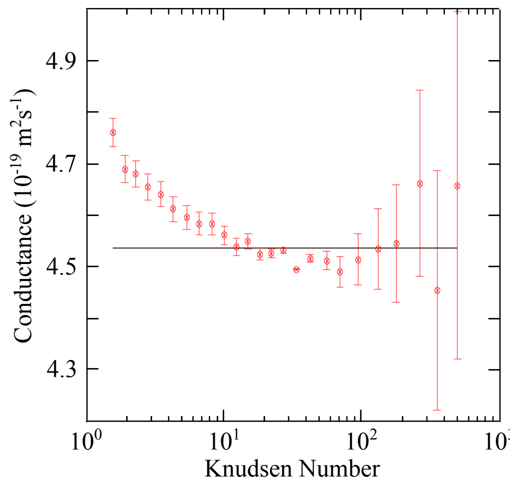

(b) Conductance.

or shrunk since the initial drilling.

Figure 5.2a shows the mass flow and conductance through the 32.4×35.2 nm nanopore displayed in Figure 5.1. The horizontal line in Figure 5.2b indicates the average conductance for all data points with Knudsen Numbers greater than 10. This conductance is equivalent to the conductance that would be expected from a nanopore with a diameter of 30.6 nm with a length to radius ratio of 5 and an angle of opening of 10°. This prediction is within 10% of the radius measured in the image.

5.2 High Pressure Tests

High pressure tests start with low pressures to test whether or not a leak might be present. Then, the pressure is increased until either the membrane breaks or until the gas handling system can no longer increase the pressure. These high pressure tests are meant to test whether or not TEM drilled nanopores can be used as de Laval nozzles that allow transonic flows.

Figure 5.3: Nanopores Used in High Pressure Tests.

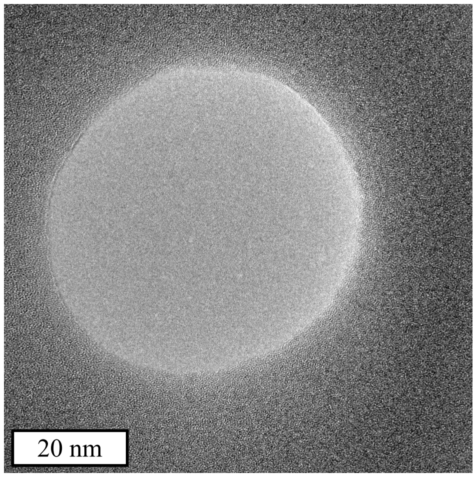

(a) Sample 2 TEM image.

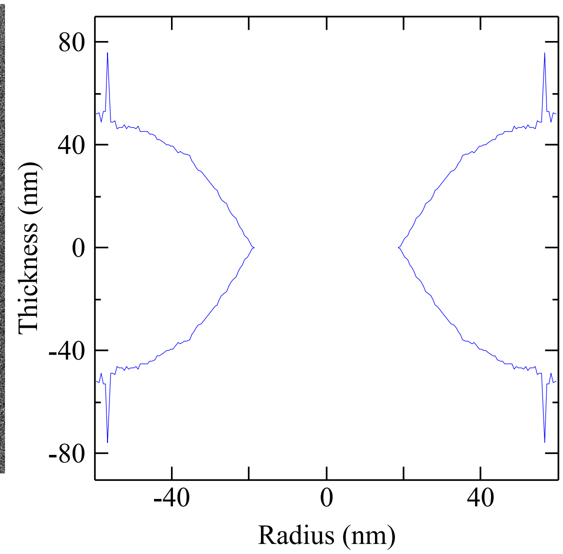

(b) Sample 2 cross section.

5.2.1 Results

There were two samples used for high presure flow tests. Sample 1 was drilled to 39.4×43.7 nm while Sample 2 was drilled to 53.6×49.7 nm. Both samples were drilled in 100 nm thick silicon nitride membranes.

Sample 1 broke at 1100 psi with the final data point taken just above 1000 psi. A linear fit was applied to the low pressure conductance and Equation 5.5 was used to calculate the radius. These results indicate a nanopore with a 38.5 nm diameter and an angle given by $\alpha = 40°$, in close agreement with the TEM image and the profile shown in Figure 4.2. The mass flow remained below choked flow for all pressures, indicating subsonic flow speeds. The final data point reached a mass flow of 85.6% of the choked flow value. Equation 3.18 was used to determine the Mach number, which was found to be $M = 0.608$. This corresponds to a velocity of 296 m/s.

Sample 2 broke above 900 psi before the flow stabilized, so the final data point is at 707 psi. The mass flow measured exceeds the calculated choked

Figure 5.4: Sample 1 high pressure data

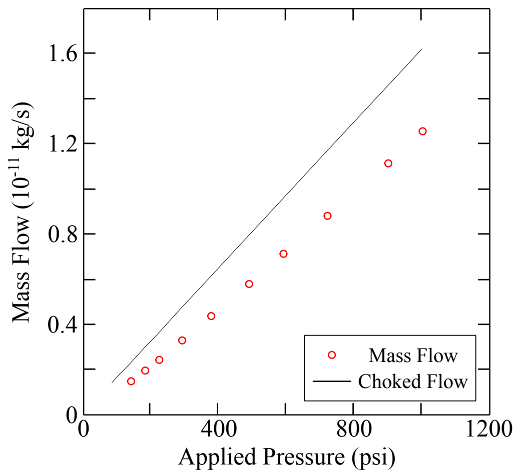

(a) Mass flow and choked flow for Sample 1

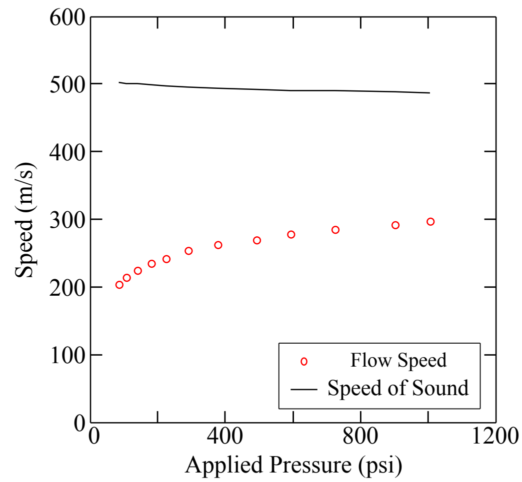

(b) Flow speed in the throat.

flow when assuming the nanopore matched the dimensions calculated from the TEM image. This indicates that the nanopore likely grew between drilling and measurements. This suspicion was confirmed by the low pressure conductance values, which indicate a diameter of 67.6 nm and and angle given by $\alpha = 25°$, using the average values of the $L/R = 5$, $\alpha = 20°$ and $\alpha = 30°$ values. Using this diameter, the choked flow is recalculated. With the new choked flow values, the mass flow remains below choked flow for all data points. The final data point reaches 87.3% of the choked flow value, with a corresponding Mach number 0.630 and a speed of 306 m/s.

While the speeds in both samples remain well below the speed of sound, thus not creating a sonic horizon, they do reach speeds of hundreds of meters per second after accelerating over a distance of only 50 nm. This implies a large acceleration that provides much higher Unruh temperatures than Unruh predicted for macroscopic (mm size) de Laval nozzles [3].

Figure 5.5: Sample 2 high pressure data

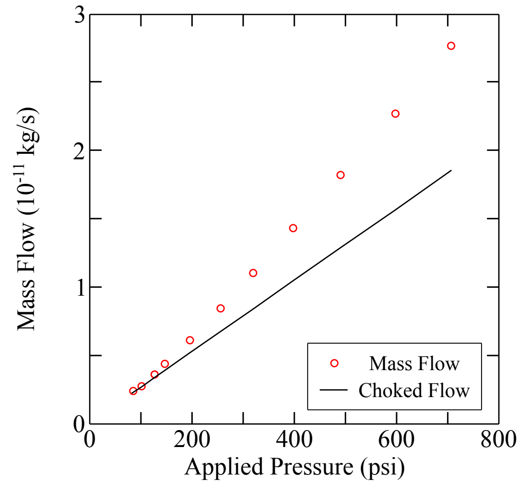

(a) Mass flow and choked flow for Sample 2 using the TEM image radius.

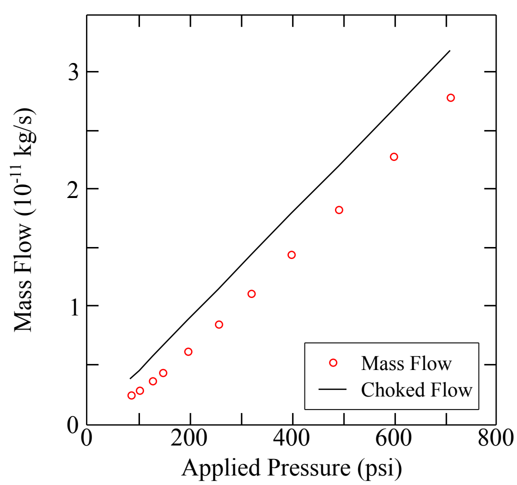

(b) Recalculated choked flow using the radius taken from low pressure conductances.

5.2.2 Phonon Temperatures

The Unruh temperatures were calculated for all data points in the high pressure flows using Equations 2.23 and 2.24. It was assumed that the narrowest point in each nozzle was exactly halfway through the thickness of the membrane and so the fluid accelerated over a distance of 50 nm before reaching its maximum speed. While the acceleration was likely not constant over the lenth of the nozzle, more information on the pressure gradients would be required to calculate the exact accelerations than is available without numerical simulations. A constant acceleration was therefore assumed and is likely a conservative estimate, as a varying acceleration would necessarily include a region of greater acceleration and thus provide a higher Unruh temperature. The calculated Unruh temperatures are shown in Figure 5.6. Samples 1 and 2 reached Unruh temperatures of 7.2×10^{-3} K, and 7.4×10^{-3} K respectively. Again, this is much larger than Unruh's previous estimate in the nK range for macroscopic nozzles [3]

The rate of phonon emission was also calculated for each sample. The

Figure 5.6: Unruh temperatures

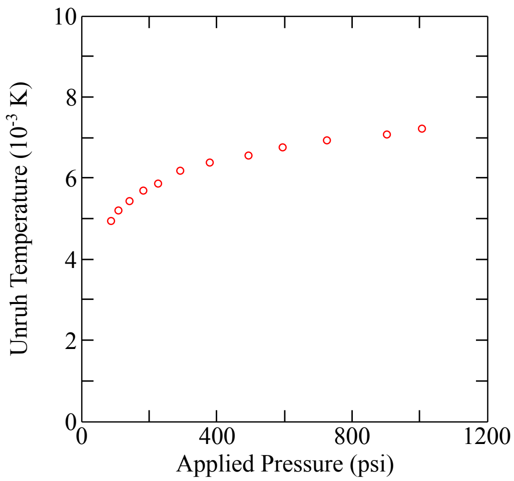

(a) Unruh temperatures of Sample 1.

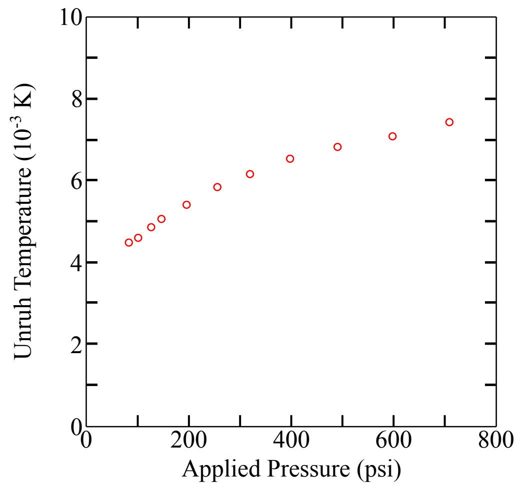

(b) Unruh temperatures of Sample 2.

Stefan-Boltzmann law,

$$j = \sigma_{sound} T^4, \tag{5.6}$$

was used to find the energy radiated per unit surface area, j, and multipled by the area A of the nanopore. T here is the Unruh temperature of the sonic black hole. The sonic Stefan-Boltzmann constant is given in [17] as

$$\sigma_{sound} = \frac{\pi^2}{120} \frac{k_B^4}{c^2 \hbar^3}. \tag{5.7}$$

This calculation assumes that the sonic black hole radiates phonons as a perfect black body with an average energy of $E = k_B T$. While this is certainly an overestimate of the phonon emission, the goal here is to simply provide an estimate regarding the number of phonons radiated. The calculated emission rates are shown in Figure 5.7. The maximum rates of emission were 3.38×10^5 Hz for Sample 1 and 1.15×10^6 Hz for Sample 2. The difference in emission rates here is primarily due to the larger area of the nanopore in Sample 2.

The Unruh temperatures and phonon emission rates calculated in this sec-

Figure 5.7: Phonon emission rates.

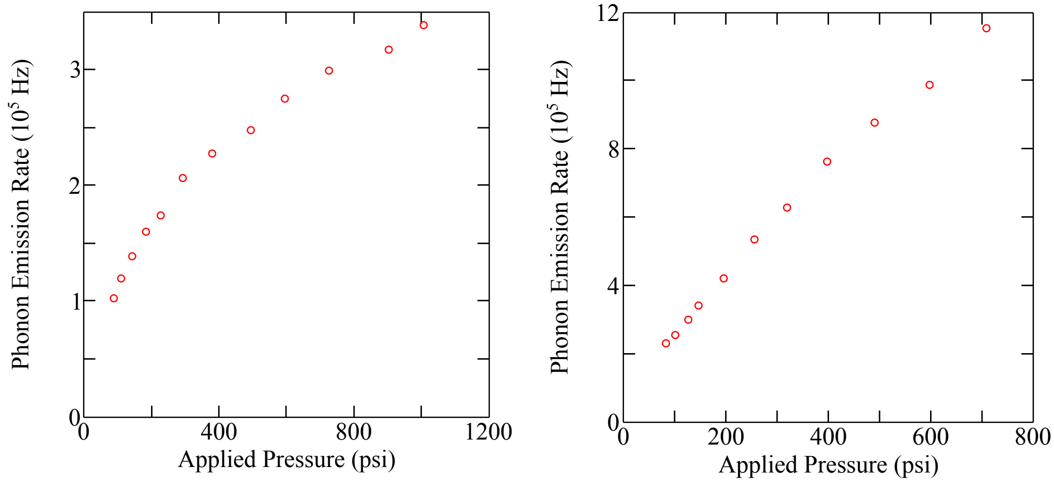

(a) Phonon emission rates of Sample 1. (b) Phonon emission rates of Sample 2.

tion are merely estimates based on a few simplifying assumptions. More detailed knowledge of the velocity gradients would be needed to provide accurate calculations of the Unruh temperature and the resulting spectrum. With knowledge of the spectrum, a precise phonon emission rate could be calculated. This has not yet been done, but this work is currently on-going. These calculations do, however, provide an order of magnitude estimate of the phonon emission rates and indicate that a sufficient number of phonons are emitted such that they could, in principle, be detected with sufficiently sensitive detectors. A precise calculation of the spectrum could also allow one to determine whether the phonons can be distinguished from the thermal background noise.

Chapter 6

Conclusion

In the present work, nanopores were drilled in 100 nm thick silicon nitride membranes using focussed transmission electron microscope (TEM) beams. The samples were placed in a stainless steel cell submerged in liquid nitrogen and had varying pressures of helium gas applied across them. Mass flows were then measured using a mass spectrometer and pressures were measured with a pressure gauge.

Based on the measured mass flow and the known pressure and temperature, the Mach number was calculated. Using available data for the speed of sound in helium, the velocity was calculated based on the Mach number [20]. These velocities were used in the equations for Unruh temperatures based the assumption of constant acceleration from the opening of the nanopore to the throat of the nozzle, midway through the membrane [5]. An estimate of the rate of phonon emission was made using the Stefan-Boltzmann law [17]. This estimate assumed that the nozzle radiated phonons as a perfect black body with an average phonon energy of $k_B T$.

Two samples were used in high pressure flow measurements. Sample 1 was drilled to 39.4×43.7 nm and Sample 2 was drilled to 53.6×49.7 nm. The final speed reached by Sample 1 was calculated to be 296 m/s, or Mach 0.608 at a pressure of 1004 psi. Sample 2 reached a maximum speed of 306 m/s, or Mach 0.630 at 707 psi. Both samples broke at higher pressures before another data point could be taken. Sample 2 likely achieved a higher maximum speed due to slight differences in the geometries of the samples.

While both samples failed to reach the speed of sound, they did achieve high accelerations by reaching speeds around 300 m/s over a distance of 50 nm. This allowed Samples 1 and 2 to reach Unruh temperatures of 7.2×10^{-3} K and 7.4×10^{-3} K respectively. These temperatures allowed the nanopores to emit phonons at rates on the order of 10^5 to 10^6 Hz.

This experiment was unable to confirm whether the TEM drilled nanopores can act as de Laval nozzles and accelerate helium gas to the speed of sound. Since neither sample approached the speed of sound, it is unknown whether this failure was due to the geometry of the nanopores or due to the fragility of the membanes preventing higher pressure gradients.

In order to determine whether TEM drilled nanopores can act sufficiently as de Laval nozzles, more precise measurements on the shape of the pores need to be made, possibly with an atomic force microscope. These measurements would then allow numerical simulations to be performed. These simulations could then determine if the flow through a nanopore can reach the speed of sound, and if so, at what pressure. It is likely that either thicker membranes or membranes with smaller surface areas will be required in order to reach pressures greater than 1000 psi.

Even if the type of nanopore used in this experiment cannot accelerate fluid to the speed of sound, they are a reasonable approach to detecting Unruh radiation. Other approaches to creating nanopores like etching will necessarily require thicker membranes and wider nozzles [31]. While these nozzles might reach greater speeds and reach the speed of sound, this would only increase the speed by a factor of 2, while the length over which the fluid accelerates might increase by a factor of 1000. This would then reduce the Unruh temperature by 500 times.

TEM drilled nanopores may not be able to provide the precise geometry control that is required to create a de Laval nozzle. This suggests that TEM drilled nanopores are not ideal as candidates for sonic black holes. They do, however, create comparitavely high accelerations and thus high Unruh temperatures, making them good candidates for detecting the Unruh effect.

Bibliography

[1] Unruh W.G. Notes on black-hole evaporation. *Physical Review D*, 14(4), 1976.

[2] Hawking S. W. Particle creation by black holes. *Communications in Mathematical Physics*, 43(3), 1975.

[3] Unruh W. G. Experimental black-hole evaporation? *Physical Review Letters*, 46(21):1351-1353, 1981.

[4] Garay L.J. Anglin J.R. Cirac J.I. and Zoller P. Sonic analog of gravitational black holes in Bose-Einstein condensates. *Physical Review Letters*, 85(22), 2000.

[5] Furuhashi H. Nambu Y. and Saida H. Simulation of an acoustic black hole in a laval nozzle.*Classical and Quantum Gravity*, 23(17):5417-5438, 2006.

[6] Weinfurtner S. Tedford E.W. Penrice M.C.J. Unruh W.G. and Lawrence G.A. Measurement of stimulated hawking emission in an analogue system. *Physical Review Letters*, 106(2), 2011.

[7] Dauphinais G. Fabrication, structural relaxation, and flow in solid-state nanopores. *McGill University*, 2011.

[8] Savard M. Tremblay-Darveau C. and Gervais G. Flow conductance of a single nanohole. *Physical Review Letters*, 103(104502), 2009,

[9] Bekenstein J.D. Black hole thermodynamics. *Physics Today*, 33, 1980.

[10] Wald R. M. Quantum field theory in curved space-time and black hole thermodynamics. *University Of Chicago Press*, 1994.

[11] Raine D. J. and Thomas, E. G. Black holes: an introduction, 2nd edition. *Imperial College Press*, 2005.

[12] Carrol S. M. Spacetime and geometry: an introduction to general relativity. *Addison Wesley*, 2004.

[13] Carlip S. Black hole thermodynamics and statistical mechanics. *Lecture Notes In Physics*, 769:89-123, 2009.

[14] Begelman M. C. Evidence for black holes. *Science*, 300(5627):1898-1903, 2003.

[15] Grøn Ø. and Hervik S. Einstein's general theory of relativity: with modern applications in cosmology. *Springer*, 2007.

[16] Unruh W.G. Dumb holes: analogues for black holes. *Philosophical Transactions of the Royal Society A: Mathematical, Physical and Engineering Sciences*, 366(1877):2905-2913, 2008.

[17] Novello M. Visser M. and Volovik G. E. Artificial black holes. *World Scientific*, 2002.

[18] Barceló C. Liberati S. Sonego S. and Visser M. Hawking-like radiation does not require a trapped region. *Physical Review Letters*, 97(17), 2006.

[19] Garay L. J. Anglin J. R. Cirac J. I. and Zoller P. Sonic black holes in dilute Bose-Einstein condensates. *Physical Review A*, 63(2), 2001.

[20] McCarty R.D. Thermodynamic properties of helium 4 from 2 to 1500 K at pressures to 100 MPa. *Journal of Physical and Chemical Reference Data*, 2(4):923-1041, 1973.

[21] Nakka R. Richard Nakka's experimental rocketry site. *http://www.nakka-rocketry.net/th_nozz.html*, 2006.

[22] *http://www.grc.nasa.gov/www/k-12/airplane/mflchk.html*

[23] Landau L. D. and Lifshitz E. M. Fluid mechanics 2nd edition. *Pergamon Press*, 1987.

[24] Zandbergen M. Zandbergen H., Wu M.-Y., Krapf D. and Batson P. E. Formation of nanopores in a SiN/SiO2 membrane with an electron beam. *Applied Physics Letters*, 87(113106), 2005.

[25] Ling X.S. Zandbergen H.W. Storm A.J. Chen J. H. and Dekker C. Fabrication of solid-state nanopores with single-nanometre precision. *Nature Materials*, 2:537-540, 2001.

[26] Murata K. Kim M. J., McNally B. and Meller A. Characteristics of solid-state nanometer pores fabricated using a transmission electron microscope. *Nanotechnology*, 18(205302), 2007.

[27] Heer C.V. Statistical mechanics, kinetic theory and stochastic process. *Academic Press*, 1972.

[28] Richardson R.C. and Smith E.N. Experimental techniques in condensed matter physics at low temperatures. *Westview Press*, 1998.

[29] Iczkowski R.P. Margrave J.L. and Robinson S.M. Effusion of gases through conical orifices. *Journal of Physical Chemistry*, 67(2):229-233, 1963.

[30] Gomez-Goni J. Lobo, J.P. Comparison between Monte Carlo and analytical calculation of the conductance of cylindrical and conical tubes *Journal of Vacuum Science & Technology A*, 21(4), 2003.

[31] Li S. Freidhoff C.B. Young R.B. Ghodssi R. Fabrication of micronozzles using low-temperature wafer-level bonding with SU-8. *Journal of Micromechanics and Microengineering*, 13(5), 2003.